On the inherent strength of $Cr_{23}C_6$ with the complex face-centered cubic $D8_4$ structure

Kyosuke Kishida[1,2,*], Mitsuhiro Ito[1], Haruyuki Inui[1,2], Martin Heilmaier[3], and Gunther Eggeler[4]

[1] Department of Materials Science and Engineering, Kyoto University
Sakyo-ku, Kyoto 606-8501, JAPAN
[2] Center for Elements Strategy Initiative for Structural Materials (ESISM), Kyoto University
Sakyo-ku, Kyoto 606-8501, JAPAN
[3]Institute for Applied Materials (IAM-WK), Karlsruhe Institute of Technology (KIT), Engelbert-Arnold-Strasse 4, 76131 Karlsruhe, Germany
[4]Lehrstuhl Werkstoffwissenschaft (WW), Institut für Werkstoffe, Ruhr-Universität Bochum, Universitätsstrasse 150, D-44780 Bochum, Germany

Abstract

The deformation behavior of single crystals of $Cr_{23}C_6$ with the complex $D8_4$ crystal structure based on the face-centered cubic lattice has been investigated by micropillar compression as a function of crystal orientation and specimen size at room temperature. For the first time, the {111}<$\bar{1}$01> slip system is identified to be the only operative slip system. The 1/2<$\bar{1}$01> dislocation dissociates into two partial dislocations with identical collinear Burgers vectors (**b**) as confirmed by transmission electron microscopy (TEM) and atomic-resolution scanning transmission electron microscopy (STEM). The energy of the stacking fault bounded by two coupled partial dislocations with the **b**=1/4<$\bar{1}$01> is evaluated from their separation distances to be 840 mJ/m^2. The critical resolved shear stress (CRSS) for {111}<$\bar{1}$01> slip increases with the decrease in the specimen size, following the inverse power-law relationship with a relatively low exponent of ~ -0.19. The room-temperature bulk CRSS value evaluated by extrapolating this inverse relationship to the specimen size of 20~30 μm is 0.79 ± 0.15 GPa. The exact position of the slip plane among many different parallel {111} atomic planes and possible dislocation dissociations on the relevant slip planes are discussed based on the calculated generalized stacking fault energy (GSFE) curves. The inter-block layer slip is deduced to occur for {111}<$\bar{1}$01> slip based on the TEM/STEM observations and the result of GSFE calculations. Finally, plausible atomic structures for stacking faults on (111) and coherent twin boundaries are discussed.

Keywords: Transition metal carbide; Deformation structure; Dislocations; Mechanical properties; Micropillar compression

*Corresponding author: Kyosuke KISHIDA
Department of Materials Science and Engineering, Kyoto University
Sakyo-ku, Kyoto 606-8501, JAPAN
E-mail address: kishida.kyosuke.6w@kyoto-u.ac.jp
Tel.: +81-75-753-5461; fax: +81-75-753-5461

1. Introduction

Carbides of type $M_{23}C_6$ (M denoting a metallic element) are key phases of microstructures of important structural materials like steels and Ni-base superalloys [1-5]. In bainitic low Cr tool steels and tempered martensitic 9-12% Cr high-temperature steels, their formation during heat treatments delays the formation of pearlite and provides more time for well controlled heat treatments [6,7]. In these steels, $M_{23}C_6$ carbides precipitate on various internal interfaces (prior austenite grain boundaries, block boundaries, lath boundaries and on subgrain boundaries to mention the most relevant). As such elements they provide what has been referred to as carbide stabilized substructure hardening in low and high Cr-steels [6,7]. Their role in the creep resistance of low and high Cr steels has been thoroughly investigated in the last decades [6-11]. They have also been reported beneficial for high Mn austenitic steel [12] as $M_{23}C_6$-type carbide particles precipitated during low-temperature ageing treatments increase the hardness and strength in these steels [13]. While austenitic stainless steels such as type 304 are also strengthened by $M_{23}C_6$-type carbide particles, those precipitated at grain boundaries are known to reduce the grain boundary Cr content, reducing the corrosion resistance along the grain boundary thereby increasing the susceptibility to stress corrosion cracking [14,15]. $M_{23}C_6$-type carbide particles are also commonly observed precipitates in Ni-based alloys after high temperature service [16,17]. While fine $M_{23}C_6$-type carbide particles are known to generally increase the creep strength [18-21], coarse $M_{23}C_6$-type carbide particles are reported to degrade the fatigue properties of Ni-based superalloys by offering crack initiation sites due to local stress concentration accumulated at the carbide/austenite interface [22-26]. A similar detrimental effect of $M_{23}C_6$-type carbide particles is reported also for high Cr ferritic steels [27]. Thus, the presence of $M_{23}C_6$ particles can have significant positive and negative effects on the strength of important structural materials. This is why effort has been devoted to study their thermal stability [28]. In contrast, only limited information is available regarding their intrinsic strength. Most researchers focusing on structural materials consider them as inert particles with a high strength, which act as obstacles for dislocation motion, boundary migration and grain boundary sliding or as stress raisers. Only Cr and Mn are known to form the binary $M_{23}C_6$-type carbide with carbon [29]. Cr is a key alloy element in bainitic and martensitic steels as well as in superalloys. Therefore, even though Mn can also form a binary carbide of type $M_{23}C_6$, $Cr_{23}C_6$ is the most relevant binary reference system for $M_{23}C_6$-type carbides.

$Cr_{23}C_6$ has a crystal structure of the $Cr_{23}C_6$-type with its own prototype name (the $D8_4$ structure in the Strukturbericht symbolism) based on the face-centered cubic (FCC) lattice. The space group is $Fm\bar{3}m$ and the Pearson's symbol is $cF116$. The lattice parameter reported is a = 1.0650 nm and the unit cell contains 92 Cr and 24 C atoms [29,30]. As shown in Fig. 1, the crystal structure is often described as made up with the packing of some coordination polyhedra, cubo-octahedra and cubes [29,30]. The cubo-octahedron is formed by 12 Cr atoms in 48*h* sites (Cr(III)) centered by a Cr atom in the 4*a* site (Cr(I)), while the cube is formed by 8 Cr atoms in 32*f* sites (Cr(IV)). Cubo-octahedra are allocated to the face-centered cubic lattice points (i.e., 4*e* sites) while cubes are allocated to the centers of octahedral gaps formed by six cubo-octahedra (i.e., to mid-points of the cube edge and the body center of the lattice). In addition, Cr atoms are allocated to the body centers of one-eights sublattices in 8*c* sites and C atoms are allocated to 24*e* sites on the cube edge between the cubo-octahedron and the cube. Each C atom is coordinated by 8 Cr atoms that form a distorted 8-fold square anti-prism. The crystallographic sites (either 48*h*, 32*f* or 8*c*) for metallic elements (such as Fe and some alloying elements like W, Mo and Mn for steel) have been investigated for decades to improve the thermal stability of $M_{23}C_6$ type carbides [31-36]. While the crystallography of $M_{23}C_6$-type carbides has been investigated by several researchers, there exists insufficient information about the mechanical properties of $M_{23}C_6$-systems. This is partly related to the difficulty to synthesize bulk monolithic $M_{23}C_6$, which in case of $Cr_{23}C_6$ forms via a peritectic reaction in a high carbon vapor pressure. Moreover, $Cr_{23}C_6$ was also expected to exhibit brittleness, another reason for not trying to assess its resistance against plastic deformation. Relatively high values of Vickers hardness (~1.1 GPa for $(Cr,Fe)_{23}C_6$ [37] and 13~15 GPa for $Cr_{23}C_6$ [38]) have been reported so far, together with relatively low values of fracture toughness (4.4~5.8 MPam$^{1/2}$ for $Cr_{23}C_6$ [38]). Recent density functional theory (DFT) calculation results [39-41] have predicted a high elastic modulus and low Poisson's ratio, indicative of the brittleness of $Cr_{23}C_6$, and a low fracture toughness [38]. Microstructure observations by transmission electron microscopy (TEM) have revealed stacking faults on {111} and {001} planes in well-annealed $Cr_{23}C_6$ doped with Fe, W, Mo and Mn [37], stacking faults on {111} and microtwins within $M_{23}C_6$ type carbides in deformed Ni-based superalloys [42] and in deformed high-Mn austenitic steel [13]. The presence of these planar faults may suggest that densely packed {111} planes can represent slip planes, consistent with what is expected from a face-centered cubic lattice, which the crystal structure of $Cr_{23}C_6$ is related to, see green atoms in Figure 1. Xia et al. [43] recently made first-principles DFT calculation of generalized stacking fault energy (GSFE) surface for {111} slip plane of $Cr_{23}C_6$ and concluded that slip should occur by the motion of $1/2\langle\bar{1}01\rangle$ dislocations dissociated into two $1/6\langle 112\rangle$ Shockley-type partial dislocations as in the case of FCC metals. Unfortunately, at present no experimental evidence is available describing the mechanisms which govern the plastic deformation of $C_{23}C_6$. Thus, there is a need to identify the operative slip systems and their critical resolved shear stresses (CRSSs). Recently, we have shown that plastic flow can successfully be observed for some hard and brittle materials even at room temperature if the specimen size is reduced from bulk to micrometer size [44-50]. Micropillar compression testing in combination with post mortem analysis of defect structures in the scanning and transmission electron microscope has proven to be a powerful technique to elucidate the deformation mechanisms of hard and brittle materials [44-54].

Scientific objective of the present work is to combine micropillar compression testing with post mortem SEM and TEM analysis to reveal the elementary mechanisms which govern plasticity of $Cr_{23}C_6$. We aim at identifying slip systems and their respective CRSSs studying the plastic deformation of single crystals of $Cr_{23}C_6$ in compression as a function of crystal orientation and specimen size at room temperature. The results are expected to close a gap in the understanding of the mechanical behavior of one of the most important microstructural elements of advanced Fe- and Ni-based structural materials.

2. Experimental Procedure

Button ingots were prepared by Ar arc-melting of high-purity Cr and C in the stoichiometric composition (Cr-17 at.% C), yielding a two-phase microstructure consisting of $Cr_{23}C_6$ and body-centered cubic (BCC) Cr (8:2 by volume). The ingots were annealed at 1200°C for 168 hours. The grain size of the $Cr_{23}C_6$ crystallites was relatively large with about 200 μm. Orientations of $Cr_{23}C_6$ crystallites were determined by electron back scatter diffraction (EBSD) in the scanning electron microscope (JEOL JSM-7001FA electron microscope). Three different loading axis orientations, $[\bar{2}67]$, $[\bar{5}89]$ and $[\bar{1}\ 2\ 14]$, were selected (See, the inset of Fig. 2). The highest Schmid factors for some possible deformation modes (slip on {111}, {110} and {100} along <110>) are listed in Table 1 for each orientation. After mechanical polishing with diamond paste and mechano-chemical polishing with colloidal silica to mirror finish, micropillar single-crystal specimens with a square cross-section having an edge length L ranging from 1.5 to 11.3 μm and a height-to-L ratio approximately equal to 2.3~4 : 1 were machined from the crystallites with a JEOL JIB-4000 focused ion beam (FIB) system. A rectangular parallelepiped shape was selected to facilitate the identification of slip planes and slip directions.

Compression tests were conducted for micropillar specimens with a flat punch indenter tip on an Agilent Technologies Nano Indenter G200 nanomechanical tester at room temperature in displacement-rate-controlled mode at a nominal strain rate of 1×10^{-4} s^{-1}. Slip planes were determined by slip trace analysis made on two orthogonal surfaces of the deformed micropillar specimen by SEM. Deformation microstructures developed in the deformed micropillars were investigated by TEM with a JEOL JEM-2100F electron microscope and scanning transmission electron microscopy (STEM) with a JEOL JEM-ARM200F electron microscope. Specimens for TEM/STEM observations were prepared by FIB-SEM in-situ lift-out technique using a FEI Quanta 3D 200i Dual-Beam system equipped with an Omniprobe nanomanipulator.

GSFE surfaces for the (111) glide planes were calculated by first-principles DFT using the Vienna ab-initio simulation package (VASP) code [55-57]. The generalized gradient approximation of Perdew-Burke-Ernzerhof (GGA-PBE) was used to treat the exchange-correlation functional [58]. The optimized lattice constants for the standard unit cell calculated with an energy cutoff of 550 eV and Monkhorst-Pack *k*-point mesh of 8×8×8 were a = 1.0559 nm, which is in good agreement with the experimental value of 1.0650 nm [30,59]. For the GSFE calculations for the (111) glide planes, supercells containing 116 atoms with the in-plane unit defined by $1/2[01\bar{1}]$ and $1/2[\bar{1}01]$ were used. The height of the supercells was fixed to 4.1577 nm including a vacuum layer of about 1.5 nm in thickness. An energy cutoff was set to be 550 eV and gamma-centered *k*-point mesh of 10 × 10 × 1 was used. All atoms were relaxed along the direction perpendicular to the glide plane so as to minimize the energy of the supercell with a given in-plane displacement.

3. Results

3.1. Stress-strain behavior and slip trace observation

Figs. 2(a)~(c) show selected stress-strain curves obtained for micropillar specimens with the $[\bar{2}67]$, $[\bar{5}89]$ and $[\bar{1}\ 2\ 14]$ orientations, respectively. The edge length L of specimens are indicated in the figures. Compression tests were stopped before failure occurs for the ease of slip line observations. For most specimens regardless of crystal orientation, yielding occurs rather smoothly followed by work-hardening with a serrated flow, which indicates the repetitive occurrence of minor strain burst events [60]. The occurrence of repetitive strain bursts suggests that the multiplication of dislocations in $Cr_{23}C_6$ may not be so difficult even at room temperature once their sources are activated, because strain bursts are usually interpreted to occur as a result of an avalanche-like collective motion of dislocations in micropillar compression tests [61,62]. The yield stresses determined as the elastic limit (indicated by arrows in Fig. 2) are generally high, exceeding about 2 GPa and tend to increase with the decrease in the specimen size, regardless of crystal orientation.

Figs. 3(a)-(c) show SEM secondary electron images of deformation structures of the micropillars with the $[\bar{2}67]$, $[\bar{5}89]$ and $[\bar{1}\ 2\ 14]$ orientations, respectively. The observations were made along the direction inclined by 30° from the loading axis. For the $[\bar{2}67]$ orientation (Fig. 3(a)), straight slip lines are clearly observed on the $(\overline{71}\ \overline{54}\,26)$ surface, while slip lines observed on the $(\bar{6}5\bar{6})$ surface are fairly faint. Slip trace analysis on the two orthogonal surfaces indicates the occurrence of slip on (111). The faint slip lines on the $(\bar{6}5\bar{6})$ surface indicates that the slip vector is contained in the $(\bar{6}5\bar{6})$ plane. Stereographic analysis reveals that the slip direction is parallel to $[\bar{1}01]$. The occurrence of the slip along $[\bar{1}01]$ parallel to the $(\bar{6}5\bar{6})$ surface is further confirmed by the resultant shape change of the micropillar specimen (Supplementary Fig. S1), i.e., an apparent shape change caused by the slip is observed on the $(\bar{6}5\bar{6})$ surface (Fig. S1(b)), while the rectangular shape is virtually maintained on the $(\overline{71}\ \overline{54}\,26)$ surface (Fig. S1(a)). The slip system thus identified to operate in the micropillar with the

$[\bar{2}67]$ orientation is $(111)[\bar{1}01]$.

For the $[\bar{5}89]$ orientation (Fig. 3(b)), straight slip traces are clearly observed on the $(\overline{25}\,\overline{28}\,11)$ surface (see also Fig. S1(c)), while very faint slip traces are observed on the $(\bar{2}1\bar{2})$ surface (Fig. S1(d)). Slip trace analysis confirms the occurrence of slip deformation on (111) along $[\bar{1}01]$. For the $[\bar{1}\ 2\ 14]$ orientation (Fig. 3(c)), many straight slip traces are clearly observed on the $(\overline{62}\ \overline{10}\ \bar{3})$ surface (Fig. S1(e)), while rather faint slip traces are observed on the $(\bar{2}13\bar{2})$ surface (Fig. S1(f)). Slip trace analysis also confirms that slip deformation occurs on (111) along $[\bar{1}01]$. The slip system thus identified to operate in a wide range of crystal orientation is $(111)[\bar{1}01]$, and this slip system is the only operative slip system in $Cr_{23}C_6$ single crystal micropillars deformed in compression at room temperature.

3.2. Dislocation structure and dissociation

Fig. 4(a) shows a bright-field STEM image of the dislocation structure observed in a thin foil cut parallel to the (111) slip plane obtained from a $[\bar{2}67]$-oriented micropillar specimen deformed to 3~4 % plastic strain. Most dislocations imaged in Fig. 4(a) are confirmed to have a Burgers vector (**b**) of $1/2[\bar{1}01]$, being consistent with the results of slip trace analysis of Fig. 3(a). Although at a first glance, these $1/2[\bar{1}01]$ dislocations seem to align along a direction about 30° inclined from the screw orientation, close inspection clearly indicates that they consist of (i) small straight segments parallel to their screw orientation and (ii) kinks that connect segmented screw dislocations. This indicates that the dislocation motion of $1/2[\bar{1}01]$ dislocations is controlled by the Peierls mechanism with the Peierls valleys lying along the screw orientation.

Figs. 4(b) and (c) show weak-beam dark-field TEM images of a dislocation with **b**=$1/2[\bar{1}01]$ in the same area taken with two different diffraction vectors (**g**). The dislocation with **b**=$1/2[\bar{1}01]$ is observed to dissociate into two partial dislocations along the entire length when imaged with **g**=$\bar{4}04$ (Fig. 4(b)) so that two screw segments are connected by a kink with edge components. By contrast, when imaged with **g**=$2\bar{4}2$ (Fig. 4(c)), both partial dislocations are simultaneously invisible. This indicates that the dislocation with **b**=$1/2[\bar{1}01]$ gliding on (111) dissociates into two partial dislocations with collinear Burgers vectors, as described below:

$$1/2[\bar{1}01] \rightarrow 1/4[\bar{1}01] + 1/4[\bar{1}01]. \tag{1}$$

This is different from the dissociation scheme usually observed for FCC metals and alloys involving two Shockley partial dislocations with non-collinear Burgers vectors, described as

$$1/2[\bar{1}01] \rightarrow 1/6[\bar{2}11] + 1/6[\bar{1}\bar{1}2]. \tag{2}$$

The two partial dislocations with **b**=$1/4[\bar{1}01]$ mentioned in eq. (1) are analyzed to be separated by a stacking fault, as we will make a more detailed discussion on the dissociation schemes in the section 4.2. The stacking fault energy estimated from the observed dissociation width (~3.7 nm) along the screw orientation with the theoretically calculated shear modulus of 137 GPa [39] is as high as ~840 mJ/m^2.

The collinear dissociation of the $1/2[\bar{1}01]$ dislocation on (111) described with eq. (1) is further confirmed by atomic-resolution high-angle annular dark-field (HAADF) STEM imaging. Figs. 5(a) and (b) show the core structure for a $1/2[\bar{1}01]$ dislocation introduced in a $[\bar{2}67]$-oriented micropillar specimen deformed to ~4 % plastic strain viewed along the $[1\bar{1}0]$ direction that makes 60° with the Burgers vector. Burgers circuit construction around the dislocation (indicated with light blue circles) confirms the displacement corresponding to the perfect dislocation in 60°-character. Fig. 5(b) is a rotated and vertically compressed image of

Fig. 5(a) so that the relative displacement between the upper and lower halves of the crystal can be seen easily from the positions of the $(11\bar{1})$ atomic planes passing through the lattice points (indicated with blue lines). The approximate positions of two coupled partial dislocations are indicated with green arrows. However, the exact positions of the partial dislocations as well as the atomic arrangement in the fault region between the two partial dislocations are difficult to be unambiguously determined, because of slight inclination of the dislocation line from the $[1\bar{1}0]$ incident-beam direction. This causes the difficulty in identifying the exact location of the slip plane. However, Burgers circuit construction around each of the two partial dislocations confirms the identical displacement of half of that of the $1/2[\bar{1}01]$ perfect dislocation. This is consistent with the dissociation scheme (1) but cannot be explained with the dissociation schemes of (2) involving Shockley partial dislocations with **b**=1/6<112>. Although the exact location of the slip plane is difficult to identify only from the HAADF-STEM images of Figs. 5(a) and (b), the location of stacking fault between the two coupled partial dislocation is considered to be between structural blocks B and C from the lower energy for stacking fault of the inter-block layer type (Fig. 5(d)) rather than of the inter-sublayer type (Fig. 5(g)). This will be discussed in more detail in the sections 4.1 and 4.2.

The dissociation scheme (1) was further confirmed by atomic-resolution STEM imaging of the core structure of a $1/2[\bar{1}01]$ screw dislocation (Fig. 6). If the dissociation scheme is assumed as eq. (2), the atom displacement corresponding to the edge component of the Shockley partial dislocation should be observed in the stacking fault region between the two coupled Shockley partial dislocations. However, no atomic displacement should be observed in the stacking fault region between two collinear partial dislocations if the dissociation scheme is of type (1), because partial dislocations are both pure screw in character. Fig. 6(a) shows a low-magnification bright-filed TEM image of screw dislocations viewed end on. They exhibit a robe contrast characteristic of end-on dislocations. Fig. 6(b) is an atomic resolution HAADF-STEM image of the core structure for a $1/2[\bar{1}01]$ screw dislocation viewed end-on. In the HAADF-STEM image, no atom displacement is observed in the stacking fault region between the two coupled partial dislocations, strongly indicating that the dislocation dissociation scheme for the $1/2[\bar{1}01]$ dislocation is according to (1) but not according to (2).

The motion of $1/2[\bar{1}01]$ dislocations in $Cr_{23}C_6$ seems to be controlled by the Peierls mechanism with the movement of screw dislocations being rate-controlling. This is similar to 1/2<111> dislocations in BCC metals and dislocations in semiconducting materials such as $1/3\langle 2\bar{1}\bar{1}0\rangle$ dislocations observed in micropillar specimens of 6*H*-SiC deformed at room temperature [45], although these move as perfect dislocations without dissociation. In that sense, the present situation is much more similar to the $1/2\langle\bar{1}01\rangle$ dislocation in Si, although the $1/2\langle\bar{1}01\rangle$ dislocation in Si dissociate into two Shockley partial dislocations according to the scheme (2) rather than (1).

3.3. Critical resolved shear stress

Values of critical resolved shear stress (CRSS) for $(111)[\bar{1}01]$ slip calculated with the yield stress values (Fig. 2) and the corresponding Schmid factor (Table 1) are plotted in Fig. 7 as a function of specimen size. The CRSS values for $(111)[\bar{1}01]$ slip tend to decrease with the increase in specimen size but do not depend much on crystal orientation at a given specimen size. The data points from all the three orientations form a single inverse power law relation with specimen size. The power-law exponent is -0.19, which is smaller (in the absolute magnitude) than those commonly observed (-0.5~-1.0 and -0.3~-0.5, respectively) for FCC and BCC metals [61-63] and comparable to those (0~-0.2) for many hard and brittle materials including semiconductors, intermetallic compounds and ceramics [44-50]. The low power law exponent of $Cr_{23}C_6$ is indicative of a high frictional (Peierls) stress.

The CRSS value obtained for micropillar specimens of FCC and BCC metals usually approaches the corresponding bulk value as the specimen size increases and the CRSS value can be regarded as the bulk one when the specimen size reaches the range of 20~30 μm [61]. Assuming the same holds true for the CRSS values for $(111)[\bar{1}01]$ slip in $Cr_{23}C_6$, we can estimate the bulk CRSS values at room temperature to be 0.79 ± 0.15 GPa based on the 95% confidence band of the power-law fitting and the specimen size L of 20~30 μm.

4. Discussion

4.1. Operative slip system

The slip system identified to operate is $(111)[\bar{1}01]$ in a wide range of crystal orientations. This slip system is the primary and probably the only operative slip system at room temperature. The selection of this slip system is reasonable, because the crystal structure of $Cr_{23}C_6$ is based on the face-centered cubic lattice. The Burgers vector of 1/2<110> is naturally selected because it is the shortest translation vector of the face-centered cubic lattice. However, the selection of the slip plane of {111} in $Cr_{23}C_6$ is not as straightforward, as in the case of the FCC structure. In the FCC structure, which is a close-packed structure, {111} is a densely packed plane with the largest lattice plane spacing in the structure. In the complex crystal structure of $Cr_{23}C_6$, by contrast, there are many different parallel {111} planes (with different interplanar spacings), on which slip along <110> can occur. So, it may be useful and instructive to consider the atomic arrangements in {111} planes and their stacking to deepen our understanding as to which {111} is selected as the slip plane in $Cr_{23}C_6$.

The stacking of the ABC-type for {111} planes, as usually described for the FCC structure, is possible also for the lattice points of the face-centered cubic lattice of $Cr_{23}C_6$. A basis attached to each of the four FCC lattice points, however, consists of 29 atoms (23 Cr and 6 carbon atoms), unlike a single atom attached to each lattice point in the FCC structure (Fig. 8(a)). Then, we can examine the atomic arrangements on many different parallel (111) planes (Figs. 8(b) and (c)). One finds out that the stacking for (111) planes can also be described as ABC-type by defining the structure-building block layers A, B and C, having the identical atomic arrangement but different stacking positions, as in the FCC structure. The block layer A, for example, is made up with sublayers α', *a* and α. The sublayer *a* consists of Cr atoms (Cr(IV) at the position 48*h*) forming a hexagonal net with one-third of the hexagonal holes occupied by a Cr atom (Cr(I) at the position 4*a*) in a regular manner (Fig. 8 (c)). The sublayers α and α', which are related with each other by 180°-rotation about the 2-fold symmetry axis parallel to $[1\bar{1}0]$ (the projection direction of Fig. 8(a)) passing through the lattice point, are further sub-divided into a few different atomic layers (Figs. 8(b) and (c)). This relation holds true also for the sublayers β and β', and for the sublayers γ and γ'. The atomic layer 1 (of the sublayer α, for example) consists of Cr atoms (Cr(III) at the position 32*f*) forming a hexagonal net and it stacks on top of the sublayer *a* to fit into one of the two hexagonal hole positions of the sublayer *a*. The atomic layer 2 consists of C atoms arranged in a Kagome net and Cr atoms (Cr(II) at the position 8*c*) allocated to all the hexagonal holes of the Kagome net. On stacking on top of the atomic layer 1, the Cr atom in the atomic layer 2 is allocated to fit into the hexagonal hole of Cr atoms in the atomic layer 1, while a set of three C atoms is allocated to coordinate with a Cr atom in the atomic layer 1. The atomic layer 3 consists of Cr atoms (Cr(IV) at the position 48*h*) arranged in a hexagonal net with a set of three coordinated Cr atoms so that the center of these three coordinated Cr atoms fits into the triangular hole of C atoms in a Kagome net of the atomic layer 2. The atomic layer 4 consists of Cr (Cr(III) at the position 32*f*) in a Kagome net, the hexagonal holes of which are allocated on top of the sets of three coordinated Cr atoms in the atomic layer 3. Thus, the sublayer α consists of the above four atomic layers (1~4). However, we believe the possibility of slip occurring within the sublayer is low because the interplanar distance between any two of these four atomic layers is too small Fig. 8(b)). The atomic arrangement in each of other sublayers can be obtained through displacing the origin of the figures of Fig. 8(c) by $1/6[11\bar{2}]$ (for *b*, β and β') and further by $1/6[11\bar{2}]$ (for *c*, γ and γ') as in the FCC structure (Fig. 8(c)). Then, the stacking of (111) of the ABC-type can be described (from the bottom of Fig. 8(a)) as,

$$\underbrace{\alpha' a \alpha}_{A}\underbrace{\beta' b \beta}_{B}\underbrace{\gamma' c \gamma}_{C},$$

where α', *a,* α are sublayers of the structure-building block layer A, while β', *b,* β are those of the layer B and γ', *c,* γ are those of the layer C.

Then, we can consider two possible (111) slip planes. They are inter-block layer slip and inter-sublayer slip. The inter-block layer slip occurs between block layers A, B and C (or between α and β', β and γ', and γ and α' sublayers), while the inter-sublayer slip occurs between sublayers within each of the block layers A, B and C (such as between *a* and α, *b* and β, and *c* and γ sublayers). We calculate GSFEs on the two different (111) slip planes to get insight into the relative ease of their occurrence, as shown Fig. 9. The GSFE maps of Figs. 9(a) and (b) correspond to those for the inter-block layer slip (between α and β', β and γ', and γ and α') and inter-sublayer slip (between *a* and α, *b* and β, and *c* and γ), respectively.

For the inter-block layer slip, we can think of two different dissociation schemes of the dislocation with $\mathbf{b}=1/2[\bar{1}01]$; the collinear-type described with (1) and the Shockley-type described with (2). However, since the crystal structure of $Cr_{23}C_6$ is complicated in comparison to the close-packed FCC structure, we can additionally consider another Shockley-type dissociation, in which the leading and trailing Shockley partial dislocations in (2) are reversed. This is described as,

$$1/2[\bar{1}01] \rightarrow 1/6[\bar{1}\bar{1}2] + 1/6[\bar{2}11]. \tag{3}$$

With the movement of the leading Shockley partial dislocation in (3), atoms in the C stacking position are displaced to the B position (instead of the A position) so that BB stacking is formed across the slip plane (Figs. 5(f)) if slip is assumed to occur above the C atomic layer on top of the B atomic layer in the ABC-type stacking of the FCC structure. The energy landscape along the displacement of possible partial dislocations with the three different dissociation schemes ((1)~(3)) are displayed in Figs. 10(a) and (b) for the inter-block layer slip and inter-sublayer slip respectively. While the maximum gradient of GSFE-displacement curves and unstable stacking fault energy do not differ so much from each other for all the three dissociation schemes, the energy of stacking fault is by far smaller for the collinear dissociation of (1) than for the two different Shockley-types (2) and (3) (Fig. 10(a)). The stacking fault energy formed by the leading collinear partial dislocation with $\mathbf{b}=1/4[\bar{1}01]$ is calculated to be 1247 mJ/m^2, which is somewhat higher than the experimentally determined value of ~840 mJ/m^2 (Fig. 4(b)). The stacking fault energies formed by dissociation of the Shockley-types (2) and (3), respectively, are as high as 3264 and 2772 mJ/m^2, indicating that dissociation of the Shockley-types (2) and (3) does not actually occur for the dislocation with $\mathbf{b}=1/2[\bar{1}01]$. Thus, slip in $Cr_{23}C_6$ is considered to occur as the inter-block layer slip by the motion of $1/2[\bar{1}01]$ dislocations dissociated into two collinear partial dislocations according to (1).

For the inter-sublayer slip, by contrast, collinear dissociation of the $1/2[\bar{1}01]$ dislocation is not expected as the stacking fault energy is as high as 2400 mJ/m^2. Instead, the stacking fault energy is calculated to be rather low (952 mJ/m^2) when dissociation of the Shockley-type of (2) occurs (Fig. 9(b) and Fig. 10 (b)). Souissi et. al. [64] recently found out the formation of low-energy stacking fault of the same type by DFT calculations as well as by atomic-resolution HAADF-STEM imaging. Xia et al. [43], who recently made GSFE calculations on (111) of

$Cr_{23}C_6$, concluded that slip should occur by the motion of $1/2\langle\bar{1}01\rangle$ dislocations dissociated according to (2) of the Shockley-type in $Cr_{23}C_6$ through comparing the maximum gradients of GSFE-displacement curves and stable and unstable stacking fault energies. To note here is that Xia et al. [43] made GSFE calculations on (111) only for the inter-sublayer slip. According to our calculation, however, there is no significant difference in the maximum gradient of GSFE-displacement curves for the three different dissociation schemes (1)~(3) and the unstable stacking fault energy is the highest for the Shockley-type dissociation of (2) (Fig. 10 (b)). Indeed, we also did not experimentally observe such characteristics of the inter-sublayer slip as dissociation of the Shockley-type (Figs. 4(b) and 6).

The reason, why slip occurs as the inter-block layer slip by the motion of $1/2[\bar{1}01]$ dislocations dissociated into two collinear partial dislocations according to (1) can, thus, be found in the existence of low-energy stacking fault that ensures the shortest partial dislocation Burgers vector ($\mathbf{b}=1/4[\bar{1}01]$ versus $\mathbf{b}=1/6[\bar{2}11]$). Hence, the Peierls stress is lowest for this type of motion.

4.2. Possible atomic structures for stacking faults and twins

4.2.1. Regulations for the stacking of sublayers

Stacking faults on {111} and twins were observed in the past studies in well-annealed $Cr_{23}C_6$ doped with Fe, W, Mo and Mn [37], in deformed Ni-based superalloys [42] and in deformed high-Mn austenitic steel [12]. It may be useful to deduce some possible atomic structures of stacking faults on {111} and twins to understand how they can be formed, based on the above-discussed possible stackings of atomic layers (block layers and sublayers). We first define some rules for the stacking of sublayers. We use the Greek sublayer (α, β and γ), Greek sublayer with a prime symbol (α', β' and γ') and roman sublayer (*a*, *b* and *c*) with G, G' and R, respectively.

(a) On top of G (α, for example), any Gs (α, β and γ) and G' with the same Greek letter with the G (α') cannot stack, but other G's (β' and γ') can do so.
(b) Below and above R (*a*, for example), only G and G' with the same Greek letters with the R (α and α') are allowed to stack, and those with Greek letters different from the R (β, β', γ and γ') are not allowed to stack.

Rule (a), on the one hand, expresses how the stacking of block layers A, B and C are actually made. This is related to the process of the partial dislocation displacement during the inter-block layer slip. Rule (b), on the other hand, is related to the process of the partial dislocation displacement during the inter-sublayer slip, as the regulation states how the stacking of sublayers is made in each of the bock layers in the crystal structure of $Cr_{23}C_6$.

4.2.2. Stacking faults

The inter-block layer stacking fault that occurs, for example, between the layers B and C, can be described as,

$$\underbrace{\alpha' a\alpha}_{A}\,\underbrace{\beta' b\beta}_{B}\underset{/}{/}\underbrace{\alpha' a\alpha}_{A}\,\underbrace{\beta' b\beta}_{B}\,\underbrace{\gamma' c\gamma}_{C}\qquad\text{(with the displacement vector of } 1/6[\bar{2}11])\quad (4a)$$

or

$$\underbrace{\alpha' a\alpha}_{A}\,\underbrace{\beta' b\beta}_{B}\underset{/}{/}\underbrace{\beta' b\beta}_{B}\,\underbrace{\gamma' c\gamma}_{C}\,\underbrace{\alpha' a\alpha}_{A}\qquad\text{(with the displacement vector of } 1/6[\bar{1}\bar{1}2])\quad (4b)$$

where / denotes the stacking fault (Figs. 5(e) and (f)). However, as the corresponding stacking fault energies are calculated to be very high (Fig. 9(a)), the stacking fault of the inter-block layer-type is considered very difficult to form both as shear fault and as growth fault.

The inter-sublayer stacking fault that occurs, for example, between the sublayers *b* and β in the layer B, can be described as,

$$\underbrace{\alpha' a\alpha}_{\mathrm{A}}\,\underbrace{\beta' b/\gamma}_{\mathrm{B}^{F}}\,\underbrace{\alpha' a\alpha}_{\mathrm{A}}\,\underbrace{\beta' b\beta}_{\mathrm{B}} \qquad \text{(with the displacement vector of } 1/6[\bar{2}11]\text{)} \tag{5a}$$

or

$$\underbrace{\alpha' a\alpha}_{\mathrm{A}}\,\underbrace{\beta' b/\alpha}_{\mathrm{B}^{F}}\,\underbrace{\beta' b\beta}_{\mathrm{B}}\,\underbrace{\gamma' c\gamma}_{\mathrm{C}} \qquad \text{(with the displacement vector of } 1/6[\bar{1}\bar{1}2]\text{)} \tag{5b}$$

where the superscript *F* indicates a block layer with a stacking fault (Figs. 5(h) and (i)). Since the corresponding stacking fault energies are relatively low, especially for the stacking fault described with (5a) (Fig. 9(b)), the stacking fault may be formed as a growth fault. Indeed, Souissi et. al. [64] recently confirmed the existence of the stacking fault of type (5a) by atomic-resolution HAADF-STEM imaging.

The present study has clarified that the inter-block layers slip occurs by the motion of $1/2\langle\bar{1}01\rangle$ dislocations dissociated into two identical collinear partial dislocations ($\mathbf{b}=1/4\langle\bar{1}01\rangle$). If the inter-block layer stacking fault is formed with the displacement vector $1/4\langle\bar{1}01\rangle$, the stacking conversion among A, B and C does not occur. If the resultant stacking is expressed with the asterisk symbol (*) with the same letters, the inter-layer stacking fault formed with this displacement vector, for example, between the layers B and C, is described as (Fig. 5(d)),

$$\underbrace{\alpha' a\alpha}_{\mathrm{A}}\,\underbrace{\beta' b\beta}_{\mathrm{B}}\,\underset{/}{/}\,\underbrace{\gamma'^{*} c^{*}\gamma^{*}}_{\mathrm{C}^{*}}\,\underbrace{\alpha'^{*} a^{*}\alpha^{*}}_{\mathrm{A}^{*}} \tag{6}$$

The stacking fault of this type is considered to form both as shear fault (as observed in the present study (Figs. 4 and 5)) and as growth fault, as the corresponding stacking fault energy and the Peierls stress for the dislocation motion are both not so high.

4.2.3. Other {111} planar faults

If the Shockley partial displacement of $\mathbf{b}=1/6\langle 11\bar{2}\rangle$ occurs synchronously on successive (111) planes, for example, between γ' and *c* and between *c* and γ within a block layer C, we can think of synchroshear for slip on (111) in $Cr_{23}C_6$, as observed in Laves-phase intermetallic compounds [65-67]. A stacking fault different from those described above is formed after the passage of the leading synchro-partial dislocation. When slip along $[\bar{1}01]$ is considered, eight different combinations of partial Burgers vectors $\mathbf{b}_1$~$\mathbf{b}_3$ can be considered, see Fig. 11. For all cases of Fig. 11, the Burgers vectors of two-coupled partials dislocations are $-\mathbf{b}_1$ and $\mathbf{b}_3$, similarly to those in the synchroshear in Laves phase compounds [65-67]. Two different types of double-layer stacking faults can be formed as described below,

$$\underbrace{\alpha' a\alpha}_{\mathrm{A}}\,\underbrace{\beta' b\beta}_{\mathrm{B}}\,\underbrace{\gamma'/b/\alpha}_{\mathrm{C}^{F}}\,\underbrace{\beta' b\beta}_{\mathrm{B}}\,\underbrace{\gamma' c\gamma}_{\mathrm{C}}\,\underbrace{\alpha' a\alpha}_{\mathrm{A}} \qquad \text{(for Figs. 11(a) - (d))} \tag{7a}$$

and

$$\underbrace{\alpha' a\alpha}_{\mathrm{A}}\,\underbrace{\beta' b\beta}_{\mathrm{B}}\,\underbrace{\gamma'/a/\beta}_{\mathrm{C}^{F}}\,\underbrace{\gamma' c\gamma}_{\mathrm{C}}\,\underbrace{\alpha' a\alpha}_{\mathrm{A}}\,\underbrace{\beta' b\beta}_{\mathrm{B}} \qquad \text{(for Figs. 11(e) - (h))} \tag{7b}$$

However, this complicated deformation mechanism may not occur in $Cr_{23}C_6$, since the Peierls stress for the motion of the Shockley partial dislocations with $\mathbf{b}=1/6\langle 11\bar{2}\rangle$ as well as the corresponding stacking fault energies are considered both (too) high.

Since $Cr_{23}C_6$ is believed to be a line compound formed via a peritectic reaction, we do not have to think of any stacking faults that cause changes in alloy chemistry. We have noticed that one way to achieve this is to remove the central pure Cr sublayers (*a*, *b* and *c*) maintaining the stacking of the upper and lower sublayers with the Greek letters. If this occurs for the *b* sublayer in the B layer, the stacking sequence will be described as follows.

$$\underbrace{\alpha' a\alpha}_{\mathrm{A}}\,\underbrace{\beta'/\beta}_{\mathrm{B}^{F}}\,\underbrace{\gamma' c\gamma}_{\mathrm{C}}\,\underbrace{\alpha' a\alpha}_{\mathrm{A}} \qquad (8)$$

This breaks the rule (a). As a result, the chemistry of the block layer B changes from $Cr_{23}C_6$ to $Cr_{18}C_6$. Although we have not observed any extended stacking faults in our specimens yet, atomic-resolution STEM imaging of extended stacking faults, if successfully found, will be the subject of our future study to identify the actual atomic arrangement of stacking fault in $Cr_{23}C_6$.

4.2.4. Twins

If the stacking fault of the type described in (4a) is introduced every inter-block layer (for example, from the layer between the block layers C and A), the stacking sequence of the block layers can be transformed into those of twin as in the case of FCC structure, as described by

$$\underbrace{\alpha' a\alpha}_{\mathrm{A}}\,\underbrace{\beta' b\beta}_{\mathrm{B}}\,\underbrace{\gamma' c\gamma}_{\mathrm{C}}\,/\,\underbrace{\beta' b\beta}_{\mathrm{B}}\,/\,\underbrace{\alpha' a\alpha}_{\mathrm{A}} \qquad (9)$$

However, a “true” twin cannot be formed simply by the passage of Shockley partial dislocations on successive inter-block layer slip planes. This is because the Greek sublayers (α, β and γ) and Greek sublayers with a prime symbol (α’, β’ and γ’) in each block layer are not correlated with mirror symmetry with respect to neither the slip plane nor to the plane perpendicular to the shear direction of the Shockley partial dislocation (Fig. 12). Thus, very complicated additional atomic shuffling to recover the crystal structure within the region sheared by the successive passage of Shockley partial dislocations would become necessary. Thus, the deformation twinning is considered to be very difficult to occur at low temperatures including room temperature.

We have found that a twin cannot be formed by introducing the $1/6<11\bar{2}>$ Shockley partial dislocation on successive inter-sublayer slip planes (5(a) and 5(b)) as well as by introducing the $1/6<11\bar{2}>$ synchro- partial dislocation on successive inter-sublayer slip planes (7(a) and 7(b)). A twin cannot be formed also by introducing $1/4<\bar{1}01>$ partial dislocations on successive inter-block layers ((6)). We thus believe that twins are very difficult to form by both, shear and growth, although micro-twins are reported to form within $M_{23}C_6$ type carbides in Ni-based superalloys [42] and in high-Mn austenitic steel [12]. If true twins are indeed introduced by high-temperature deformation, diffusion at this high temperature may possibly promote the complicated atomic shuffling occurring after or simultaneously with the successive passage of Shockley partial dislocations. Alternatively, the deformation mechanism (dislocation dissociation scheme) at high temperature may differ from that at room temperature deduced in the present study.

5. Conclusions

The micropillar compression behavior of single crystals of $Cr_{23}C_6$ with the complex *D*84 crystal structure, derived from a face-centered cubic superlattice has been investigated as a function of crystal orientation and pillar size at room temperature. The results obtained in the present work can be summarized as follows:

(1) The $\{111\}<\bar{1}01>$ slip system is identified to be the only operative slip system. $1/2<\bar{1}01>$ dislocations glide on {111} planes, which promote the alignment of dislocation segments along screw orientation This implies the presence of a high Peierls stress to be overcome. The $1/2<\bar{1}01>$ dislocations dissociate into two fault-coupled partial dislocations with identical collinear Burgers vectors of type **b**=$1/4<1\bar{1}0>$. The energy of the stacking fault bounded by two coupled partial dislocations is evaluated from their separation distances to be about 840 mJ/m^2, which is reasonably close to the results of first-principle calculations of generalized stacking fault

energies (GSFE) in this study.

(2) The critical resolved shear stress (CRSS) for $\{111\}<\bar{1}01>$ slip increases with the decrease in specimen size, following the inverse power law relationship with a relatively low exponent of ~ -0.19, which is much smaller than the value of ~ -0.5 often reported for conventional metals and alloys with FCC and BCC structures and comparable to those for the other hard and brittle materials. The bulk CRSS value at room temperature evaluated by extrapolating the inverse power law relationship to the specimen size of 20~30 μm is 0.79 ± 0.15 GPa.

(3) The exact position of the slip plane among many different parallel {111} atomic planes and possible dislocation dissociations on the relevant slip plane are discussed based on the calculated GSFE curves. The selection of the inter-block layer slip for $\{111\}<\bar{1}01>$ slip is highly probable based on the results obtained by atomic resolution HAADF-STEM imaging and GSFE calculations. Then, plausible atomic structures for stacking faults on (111) and coherent twin boundaries are discussed based on the expected dislocation motion on the deduced slip plane.

(4) Further work is recommended to study (i) the effect of temperature and (ii) chemical composition on the resistance against plastic deformation.

Acknowledgements

This work was supported by Grant-in-Aids for Scientific Research on innovative Areas on High Entropy Alloys through the grant number JP18H05450 and JP18H05451, in part by JSPS KAKENHI (grant numbers JP18H05478, JP19H00824, JP20K21084, JP21H01651, JP21K18825 and JP22H00262), the Elements Strategy Initiative for Structural Materials (ESISM) from the Ministry of Education, Culture, Sports, Science and Technology (MEXT) of Japan (grant number JPMXP0112101000) and JST CREST (grant number JPMJCR1994). HI, MH and GE acknowledge the support from the Alexander von Humboldt Foundation for their cooperative research conducted under the Humboldt Fellowship of HI.

References

[1] H.K.D.H. Bhadeshia, Bainite in Steels, Transformations, Mirostructure and Properties, 2nd Edition, The Institute of Materials, London, 1992.

[2] K.H. Lo, C.H. Shek, J.K.L. Lai, Recent developments in stainless steels, Mater. Sci. Eng. R, 65 (2009) 39-104. http://dx.doi.org/10.1016/j.mser.2009.03.001

[3] G. Krauss, Steels: Processing, Structure, and Performance, 2nd Edition, ASM International, Warrendale, 2015.

[4] C. T. Sims, A History of Superalloy Metallurgy for Superalloy Metallurgists, in: M. Gell et al. (Eds.), Superalloys 1984, TMS, Warrendale (1984) 399-419.

[5] R.C. Reed, The Superalloys, Fundamental and Applications, Cambridge University Press, Cambridge, 2006.

[6] A. Kostka, K.G. Tak, R.J. Helmig, Y. Estrin, G. Eggeler, On the contribution of carbides and micrograin boundaries to the creep strength of tempered martensite ferritic steels, Acta Mater., 55 (2007) 539-550. https://doi.org/10.1016/j.actamat.2006.08.046

[7] H. Wang, A. Kostka, W.E. Gosen, G. Eggeler, J.E. Westraad, TEM replica and particle phases in a tempered martensite ferritic steel after long term creep, Materials Characterization, 181 (2021) 111396. https://doi.org/10.1016/j.matchar.2021.111396

[8] E. Tkachev, A. Belyakov, and R. Kaibyshev, Creep behavior and microstructural evolution of a 9% Cr steel with high B and low N contents, Mater. Sci. Eng. A, 725 (2018) 228–241. https://doi.org/10.1016/j.msea.2018.04.032

[9] N. Dudova, R. Mishnev, and R. Kaibyshev, Creep behavior of a 10% Cr heat-resistant martensitic steel with low nitrogen and high boron contents at 650°C, Mater. Sci. Eng.

A, 766, (2019) 138353. https://doi.org/10.1016/j.msea.2019.138353

[10] E. Tkachev, A. Belyakov, and R. Kaibyshev, Creep strength breakdown and microstructure in a 9% Cr steel with high B and low N contents, Mater. Sci. Eng., A 772 (2020) 138821. https://doi.org/10.1016/j.msea.2019.138821

[11] E. S. Tkachev, A. N. Belyakov, R. O. Kaibyshev, The role of deformation in coagulation of $M_{23}C_6$ carbide particles in 9% Cr steel, Phys. Metals Metallogr. 121 (2020) 804-810. https://doi.org/10.1134/S0031918X20060162

[12] Z. Xu, Z. Ding, L. Dong, B. Liang, Characterization of $M_{23}C_6$ Carbides precipitating at grain boundaries in 100Mn13 steel, Metall. Mater. Trans. A, 47 (2016) 4862-4863. http://dx.doi.org/10.1007/s11661-016-3656-7

[13] L. Zheng, X. Hu, X. Kang, D. Li, Precipitation of $M_{23}C_6$ and its effect on tensile properties of 0.3C–20Cr–11Mn–1Mo–0.35N steel, Mater. Des., 78 (2015) 42–50. http://dx.doi.org/10.1016/j.matdes.2015.04.016

[14] E.C. Bain, R.H. Aborn, J.J.B. Rutherford, The nature and prevention of intergranular corrosion in austenitic stainless steels, Trans. Am. Soc. Steel Treat., 21 (1933) 481-509.

[15] B. D. Miller, Precipitation behavior of $M_{23}C_6$ carbides in type 304 stainless steel containing delta ferrite, Microsc. Microanal. 18 (2012) 1352-1353. https://doi.org/10.1017/S1431927612008616

[16] T.M. Angeliu, G.S. Was, Behavior of grain boundary chemistry and precipitates upon thermal treatment of controlled purity alloy 690, Metall. Mater. Trans. A 21, 2097–2107 (1990). https://doi.org/10.1007/BF02647868

[17] Y.S. Lim, J.S. Kim, H.P. Kim, H.D. Cho, The effect of grain boundary misorientation on the intergranular $M_{23}C_6$ carbide precipitation in thermally treated Alloy 690, J. Nucl. Mater., 335 (2004) 108-114. https://doi.org/10.1016/j.jnucmat.2004.07.038

[18] L.Z. He, Q. Zhang, X.F. Sun, G.C. Hou, H.R. Guan, Z.Q. Hu, $M_{23}C_6$ precipitation behavior in a Ni-base superalloy M963, J. Mater. Sci., 40 (2005) 2959-2964. https://doi.org/10.1007/s10853-005-2418-5

[19] G. Bai, J. Li, Z. Tang, X. Xue, H. Fu, Effect of temperature on tensile behavior of Ni–Cr–W based superalloy, Mater. Sci. Eng. A, 528 (2011) 1974-1978. https://doi.org/10.1016/j.msea.2010.11.053

[20] R. Hu, G. Bai, J. Li, J. Zhang, T. Zhang, H. Fu, Precipitation behavior of grain boundary $M_{23}C_6$ and its effect on tensile properties of Ni–Cr–W based superalloy, Mater. Sci. Eng. A, 548 (2012) 83-88. https://doi.org/10.1016/j.msea.2012.03.092

[21] L. Zheng, X. Hu, X. Kang, D. Li, Precipitation of $M_{23}C_6$ and its effect on tensile properties of 0.3C–20Cr–11Mn–1Mo–0.35N steel, Mater. Des., 78 (2015) 42-50. https://doi.org/10.1016/j.matdes.2015.04.016

[22] A. Malekbarmi, S. Zangeneh, A. Roshani, Assessment of premature failure in a first stage gas turbine nozzle, Eng. Fail. Anal., 18 (2011) 1262-1271. https://doi.org/10.1016/j.engfailanal.2011.03.011

[23] L. Jiang, R. Hu, H. Kou, J. Li, G. Bai, H. Fu, The effect of $M_{23}C_6$ carbides on the formation of grain boundary serrations in a wrought Ni-based superalloy, Mater. Sci. Eng. A, 536 (2012) 37-44. https://doi.org/10.1016/j.msea.2011.11.060

[24] L. Luo, X. Wei, J. Chen, Grain boundary carbides evolution and their effects on mechanical properties of Ni 690 strip weld metal at elevated temperature, in S. Chen, Y. Zhang, Z. Feng (eds.), Transactions on Intelligent Welding Manufacturing, Vol. II, No. 1, Springer, Singapore (2018) 73-86. https://doi.org/10.1007/978-981-10-8740-0_4

[25] S. Suresh, Fatigue of materials, 2nd. ed., Cambridge University Press, Cambridge, 1998. https://doi.org/10.1017/CBO9780511806575

[26] F. Alexandre, S. Deyber, A. Pineau, Modelling the optimum grain size on the low cycle fatigue life of a Ni based superalloy in the presence of two possible crack initiation sites,

Scripta Mater., 50 (2004) 25-30. https://doi.org/10.1016/j.scriptamat.2003.09.043

[27] J. Vivas, C. Capdevila, E. Altstadt, M. Houska, I. Sabirov, D. San‑Martín, Microstructural degradation and creep fracture behavior of conventionally and thermomechanically treated 9% chromium heat resistant steel, Metals Mater. Int., 25 (2019) 343-352. https://doi.org/10.1007/s12540-018-0192-6

[28] A. Aghajani, C. Somsen, G. Eggeler, On the effect of long term creep on the microstructure of a 12% chromium tempered martensite ferritic steel, Acta Mater., 57 (2009) 5093-5106. https://doi.org/10.1016/j.actamat.2009.07.010

[29] S. Nagakura, S. Oketani, Structure of transition metal carbides, Trans. ISIJ, 8 (1968) 265-294. https://doi.org/10.2355/isijinternational1966.8.265

[30] A.L. Bowman, G.P. Arnold, E.K. Storms, N.G. Nereson, The crystal structure of $Cr_{23}C_6$, Acta Cryst., B28 (1972) 3102-3103. https://doi.org/10.1107/S0567740872007526

[31] J.Y. Xie, N.X. Chen, L.D. Teng, S. Seetharaman, Atomistic study on the site preference and thermodynamic properties for $Cr_{23-x}Fe_xC_6$, Acta Mater., 53 (2005) 5305-5312. https://doi.org/10.1016/j.actamat.2005.07.039

[32] J. Xie, J. Shen, N. Chen, S. Seetharaman, Site preference and mechanical properties of $Cr_{23-x}T_xC_6$ and $Fe_{23-x}T_xC_6$ (T=Mo, W), Acta Mater., 54 (2006) 4653-4658. https://doi.org/10.1016/j.actamat.2006.03.059

[33] J.J. Han, C.P. Wang, X.J. Liu, Y. Wang, Z.-K. Liu, First-principles calculation of structural, mechanical, magnetic and thermodynamic properties for γ-$M_{23}C_6$ (M = Fe, Cr) compounds, J. Phys.: Cond. Mat. 24 (2012) 505503. http://dx.doi.org/10.1088/0953-8984/24/50/505503

[34] N.I. Medvedeva, D.C. Van Aken, J.E. Medvedeva, Stability of binary and ternary $M_{23}C_6$ carbides from first principles, Comp. Mater. Sci., 96 (2015) 159-164. https://doi.org/10.1016/j.commatsci.2014.09.016

[35] Y. Yi, W. Xu, F. Xia, T. Gang, L. Chen, Effects of alloying elements M (M = Fe, Mo) on phase stability of $Cr_{23}C_6$ carbides from first-principles, Adv. Eng. Res. 121 (2017) 74-80. https://doi.org/10.2991/icammce-17.2017.17

[36] M. Souissi, M.H.F. Sluiter, T. Matsunaga, M. Tabuchi, M.J. Mills, R. Sahara, Effect of mixed partial occupation of metal sites on the phase stability of γ-$Cr_{23-x}Fe_xC_6$ (x=0-3) carbides, Sci. Rep., 8 (2018) 7279. https://doi.org/10.1038/s41598-018-25642-y

[37] A. Inoue, S. Arakawa, T. Masumoto, Effect of alloying elements on defect structure and hardness of $M_{23}C_6$ type carbides, Trans. JIM, 20 (1979) 585-592. https://doi.org/10.2320/matertrans1960.20.585

[38] K. Hirota, K. Mitani, M. Yoshinaka, O. Yamaguchi, Simultaneous synthesis and consolidation of chromium carbides (Cr_3C2, Cr_7C_3 and $Cr_{23}C_6$) by pulsed electric-current pressure sintering, Mater. Sci. Eng. A, 399 (2005) 154-160. https://doi.org/10.1016/j.msea.2005.02.062

[39] C. Jiang, First-principles study of structural, elastic, and electronic properties of chromium carbides, Appl. Phys. Lett. 92 (2008) 041909. https://doi.org/10.1063/1.2838345

[40] Y. Li, Y. Gao, B. Xiao, T. Min, Y. Yang, S. Ma, D. Yi, The electronic, mechanical properties and theoretical hardness of chromium carbides by first-principles calculations, J. Alloys Comp. 509 (2011) 5242–5249. https://doi.org/10.1016/j.jallcom.2011.02.009

[41] Y. Liu, Y. Jiang, J. Xing, R. Zhou, J. Feng, Mechanical properties and electronic structures of $M_{23}C_6$ (M . Fe, Cr, Mn)-type multicomponent carbides, J. Alloys Comp. 648 (2015) 874-880. https://doi.org/10.1016/j.jallcom.2015.07.048

[42] Y.H. Rong, Y.X. Guo, G.X. Hu, Characterization of $M_{23}C_6$ carbide precipitated at grain boundaries in a superalloy, Metallography, 22 (1989) 47-55.

https://doi.org/10.1016/0026-0800(89)90021-9

[43] F. Xia, W. Xu, L. Chen, S. Wu, M.D. Sangid, Generalized stacking fault energies of $Cr_{23}C_6$ carbide: A first-principles study, Comp. Mater. Sci. 158 (2019) 20-25. https://doi.org/10.1016/j.commatsci.2018.11.006

[44] K. Kishida, T. Maruyama, H. Matsunoshita, T. Fukuyama, H. Inui, Micropillar compression deformation of single crystals of Mo_5SiB_2 with the tetragonal $D8_l$ structure, Acta Mater., 159 (2018) 416-428. https://doi.org/10.1016/j.actamat.2018.08.048

[45] K. Kishida, Y. Shinkai and H. Inui, Room temperature deformation of 6H-SiC single crystals investigated by micropillar compression, Acta Mater., 187 (2020), 19-28. https://doi.org/10.1016/j.actamat.2020.01.027

[46] Z.H. Chen, B. Paul, S. Majumdar, N.L. Okamoto, K. Kishida, H. Inui, S. Otani, Room-temperature deformation of ZrB_2 and TiB_2 with the hexagonal AlB_2 structure investigated by micropillar compression, Sci. Rep., 11 (2021) 14265. https://doi.org/10.1038/s41598-021-93693-9

[47] K. Kishida, M. Okutani, H. Inui, Room-temperature deformation of single crystals of transition-metal disilicides ($TMSi_2$) with the $C11_b$ (TM = Mo) and C40 (TM = V, Cr, Nb and Ta) structures investigated by micropillar compression, Acta Mater. 223 (2022) 117468. https://doi.org/10.1016/j.actamat.2021.117468

[48] K. Kishida, H. Suzuki, M. Okutani, H. Inui, Room-temperature plastic deformation of single crystals of α-manganese – hard and brittle metallic element, Int. J. Plasticity 160 (2023) 103510. https://doi.org/10.1016/j.ijplas.2022.103510

[49] K. Kishida, M. Okutani, H. Suzuki, H. Inui, M. Heilmaier, D. Raabe, Room-temperature deformation of single crystals of the sigma-phase compound FeCr with the tetragonal $D8_b$ structure investigated by micropillar compression, Acta Mater., 249 (2023) 118829. https://doi.org/10.1016/j.actamat.2023.118829

[50] K. Kishida, M. Morisaki, M. Ito, Z. Wang, H. Inui, Room-temperature deformation of single crystals of WC investigated by micropillar compression, Acta Mater., 260 (2023) 119302. https://doi.org/10.1016/j.actamat.2023.119302

[51] F. Östlund, P.R. Howie, R. Ghisleni, S. Korte, K. Leifer, W.J. Clegg, J. Michler, Ductile-brittle transition in micropillar compression of GaAs at room temperature, Philos. Mag., 91 (2011) 1190-1199. https://doi.org/10.1080/14786435.2010.509286

[52] S. Korte, W.J. Clegg, Discussion of the dependence of the effect of size on the yield stress in hard materials studied by microcompression of MgO, Philos. Mag., 91 (2011) 1150-1162. https://doi.org/10.1080/14786435.2010.505179

[53] S. Korte-Kerzel, Microcompression of brittle and anisotropic crystals: recent advances and current challenges in studying plasticity in hard materials, MRS Comm. **7** (2017) 109-120. https://doi.org/10.1557/mrc.2017.15

[54] S. Schröders, S. Sandlöbes, C. Birke, M. Loeck, L. Peters, C. Tromas, S. Korte-Kerzel, Room temperature deformation in Fe_7Mo_6 μ-phase, Int. J. Plasticity 108 (2018) 125-143. https://doi.org/10.1016/j.ijplas.2018.05.002

[55] V. Vitek, Intrinsic stacking faults in body-centered cubic crystals, Philos. Mag. 18 (1968) 773-786. https://doi.org/10.1080/14786436808227500

[56] V. Vitek, V. Paidar, Chapter 87, Non-planar dislocation cores: a ubiquitous phenomenon affecting mechanical properties of crystalline materials, in: J. P. Hirth (Ed.), Dislocations in Solids, Vol. 14, Elsevier, Amsterdam, 2008, pp. 441-514. https://doi.org/10.1016/S1572-4859(07)00007-1

[57] G. Kresse, J. Furthmüller, Efficient iterative schemes for *ab initio* total-energy calculations using a plane-wave basis set, Phys. Rev. B 54 (1996) 11169-11186. https://doi.org/10.1103/PhysRevB.54.11169

[58] J.P. Perdew, K. Burke, M. Ernzerhof, Generalized gradient approximation made simple,

Phys. Rev. Lett. 77 (1996) 3865-3868. https://doi.org/10.1103/PhysRevLett.77.3865

[59] H.J. Monkhost, J.D. Pack, Special points for Brillouin-zone integrations, Phys. Rev. B 13 (1976) 5188-5192. https://doi.org/10.1103/PhysRevB.13.5188

[60] S.M. Han, T. Bozorg-Grayeli, J.R. Groves, W.D. Nix, Size effects on strength and plasticity of vanadium nanopillars, Scripta Mater., 63 (2010) 1153-1156. http://dx.doi.org/10.1016/j.scriptamat.2010.08.011

[61] D.M. Dimiduk, M.D. Uchic, T.A. Parthasarathy, Size-affected single-slip behavior of pure nickel microcrystals, Acta Mater., 53 (2005) 4065-4077. https://doi.org/10.1016/j.actamat.2005.05.023

[62] M.D. Uchic, P.A. Shade, D.M. Dimiduk, Plasticity of micrometer-scale single crystals in compression, Annu. Rev. Mater. Res., 39 (2009) 161-186. https://doi.org/10.1146/annurev-matsci-082908-145422

[63] A.S. Schneider, D. Kaufmann, B.G. Clark, C.P. Frick, P.A. Gruber, R. Mönig, O. Kraft, E. Arzt, Correlation between critical temperature and strength of small-scale bcc pillars, Phys. Rev. Let. 103 (2009) 105501-1-4. https://doi.org/10.1103/PhysRevLett.103.105501

[64] M. Souissi, M.H.F. Sluiter, T. Matsunaga, M. Mabuchi, M.J. Mills, R. Sahara, Direct observation and modeling of growth-induces stacking fault in chromium-rich γ-$M_{23}C_6$ carbide, Scripta Mater., 178 (2020) 290-294. https://doi.org/10.1016/j.scriptamat.2019.11.050

[65] P.M. Hazzledine, P. Pirouz, Synchroshear transformations in Laves phases, Scripta Metall. Mater., 28 (1993) 1277-1282. https://doi.org/10.1016/0956-716X(93)90468-8

[66] M.F. Chisholm, S. Kumar, P. Hazzledine, Dislocations in complex materials, Science, 307 (2005) 701-703. https://doi.org/10.1126/science.1105962

[67] J. Guénolé, F.Z. Mouhib, L. Huber, B. Grabowski, S. Korte-Kerzel, Scripta Mater., 166 (2019) 134-138. https://doi.org/10.1016/j.scriptamat.2019.03.016

Figure captions

Fig. 1. Crystal structure of $Cr_{23}C_6$. (a) atomic arrangement in the unit cell (b) packing of cubo-octahedra, 8-fold square anti-prisms and cubes.

Fig. 2. Typical stress-strain curves obtained by micropillar compression tests for $Cr_{23}C_6$ single crystals with (a) $[\bar{2}67]$, (b) $[\bar{5}89]$ and (c) $[\bar{1}\ 2\ 14]$ orientations. Arrows indicate the yield points deduced as the elastic limit.

Fig. 3. SEM secondary electron images of deformed micropillar specimens taken diagonally from the above (inclined by 30° from the loading axis) for (a) $[\bar{2}67]$, (b) $[\bar{5}89]$ and (c) $[\bar{1}\ 2\ 14]$ orientations.

Fig. 4. (a) Bright-field STEM image of dislocation structure observed in a thin foil cut parallel to the (111) slip plane from a $[\bar{2}67]$-oriented micropillar specimen deformed to 3~4% plastic strain. (b) and (c) are weak-beam dark-field TEM images of the same area for dislocations with $\mathbf{b}$=1/2$[\bar{1}01]$ taken with (b) $\mathbf{g}$=$\bar{4}04$ and (c) $\mathbf{g}$=$2\bar{4}2$, respectively.

Fig. 5. (a) HAADF-STEM image of the core structure for a 60°-dislocation with $\mathbf{b}$=1/2$[\bar{1}01]$ introduced in a $[\bar{2}67]$-oriented micropillar specimen deformed to 3~4 % plastic strain. (b) rotated and vertically compressed image of (a) containing the stacking fault between the two partial dislocations with $\mathbf{b}$=1/4$[\bar{1}01]$. Schematic illustrations of (c) stacking positions and possible dissociation schemes and (d-i) possible atomic structure of between the two partial dislocations.

Fig. 6. (a) Bright-field TEM image of screw dislocations in a TEM foil cut perpendicular to the screw orientation $[\bar{1}01]$ from a $[\bar{2}67]$-oriented micropillar specimen deformed to 3~4 % plastic strain. (b) Atomic resolution HAADF-STEM image of a screw dislocation in marked area in (a).

Fig. 7. CRSS values for (111)$[\bar{1}01]$ slip plotted as a function of specimen size. The CRSS values are collected from micropillar single crystals with the three different loading orientations of $[\bar{2}67]$ (red circles), $[\bar{5}89]$ (blue diamonds) and $[\bar{1}\ 2\ 14]$ (green squares). Light blue band corresponds to the 95% confidence band of the power-law fitting

Fig. 8. (a) The $[1\bar{1}0]$ projection of crystal structure of $Cr_{23}C_6$ with the ABC-type stacking of the (111) plane. The outline of the unit cell and a basis attached to a lattice point are indicated with thick black rectangle and blue dotted circle, respectively. (b) Enlargement of the block layer A in (a) with subdivision of a several different parallel (111) planes. (c) Atomic arrangement of each of (111) planes defined in (b).

Fig. 9. Generalized stacking fault energy map calculated on (111) for (a) inter-block layer slip and (b) inter-sublayer slip. (c) Schematic illustration of the exact locations of the (111) slip plane for inter-block layer slip ($(111)_a$) and inter-sublayer slip ($(111)_b$).

Fig. 10. The calculated GSFE-displacement curves along the possible slip directions for (a) inter-block layer slip and (b) inter-sublayer slip.

Fig. 11. Possible double-layer stacking faults introduced by synchroshear with eight different combinations of partial Burgers vectors for (a)-(d) inter-block layer slip and (e)-(h) inter-sublayer slip.

Fig. 12. Atomic structure change after the passage of three Shockley partial dislocations on three successive inter-block layer slip planes.

Table 1. The highest Schmid factor values for some possible slip systems in $Cr_{23}C_6$ single crystals with three different loading-axis orientations tested in this study.

	Highest Schmid factor		
Loading axis	$\{111\}\langle\bar{1}01\rangle$	$\{101\}\langle\bar{1}01\rangle$	$\{010\}\langle\bar{1}01\rangle$
$[\bar{2}67]$	0.454	0.253	0.445
$[\bar{5}89]$	0.403	0.165	0.487
$[\bar{1}\ 2\ 14]$	0.457	0.485	0.148

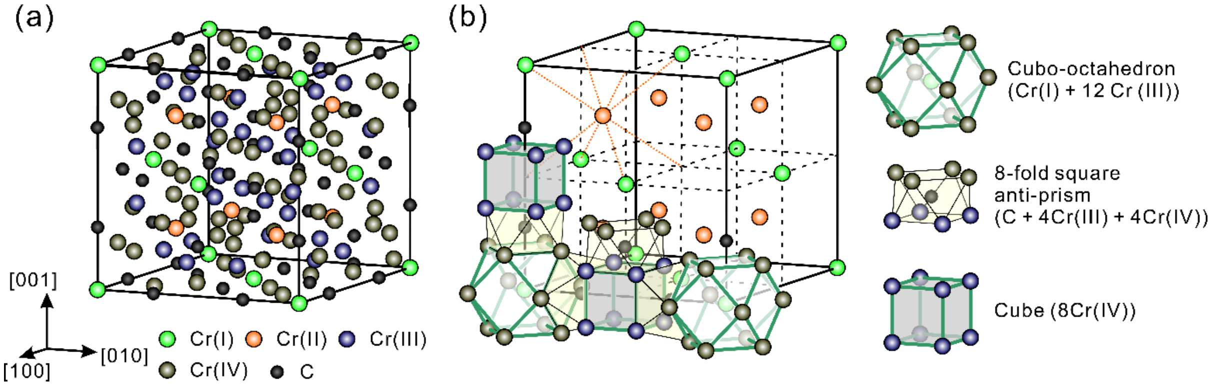

Fig. 1. Crystal structure of $Cr_{23}C_6$. (a) atomic arrangement in the unit cell (b) packing of cubo-octahedra, 8-fold square anti-prisms and cubes.

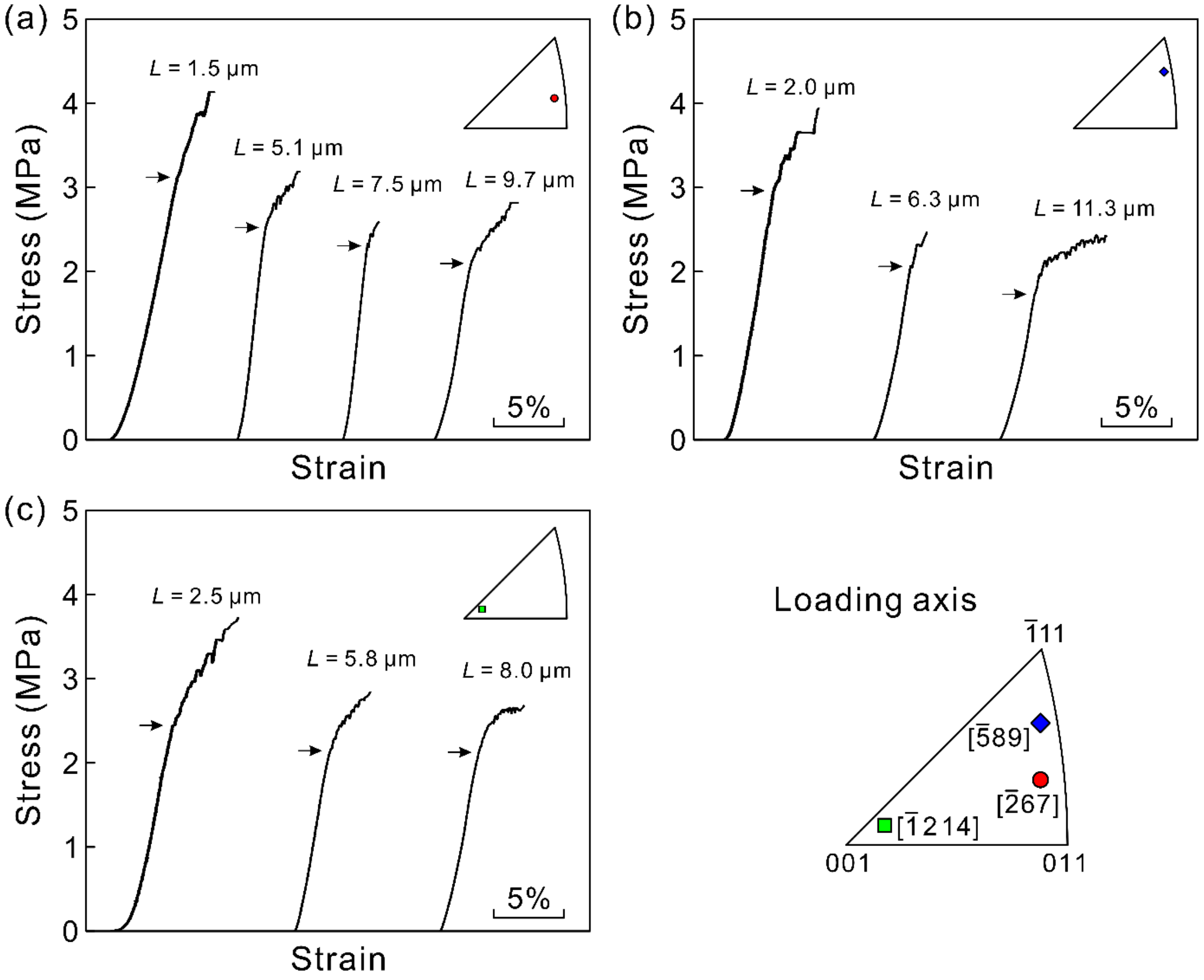

Fig. 2. Typical stress-strain curves obtained by micropillar compression tests for $Cr_{23}C_6$ single crystals with (a) $[\bar{2}67]$, (b) $[\bar{5}89]$ and (c) $[\bar{1}\ 2\ 14]$ orientations. Arrows indicate the yield points deduced as the elastic limit.

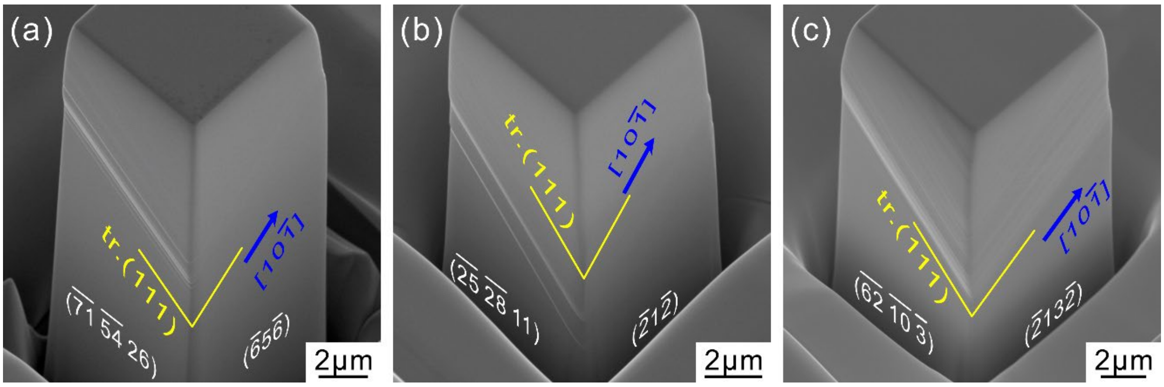

Fig. 3. SEM secondary electron images of deformed micropillar specimens taken diagonally from the above (inclined by 30° from the loading axis) for (a) $[\bar{2}67]$, (b) $[\bar{5}89]$ and (c) $[\bar{1}\ 2\ 14]$ orientations.

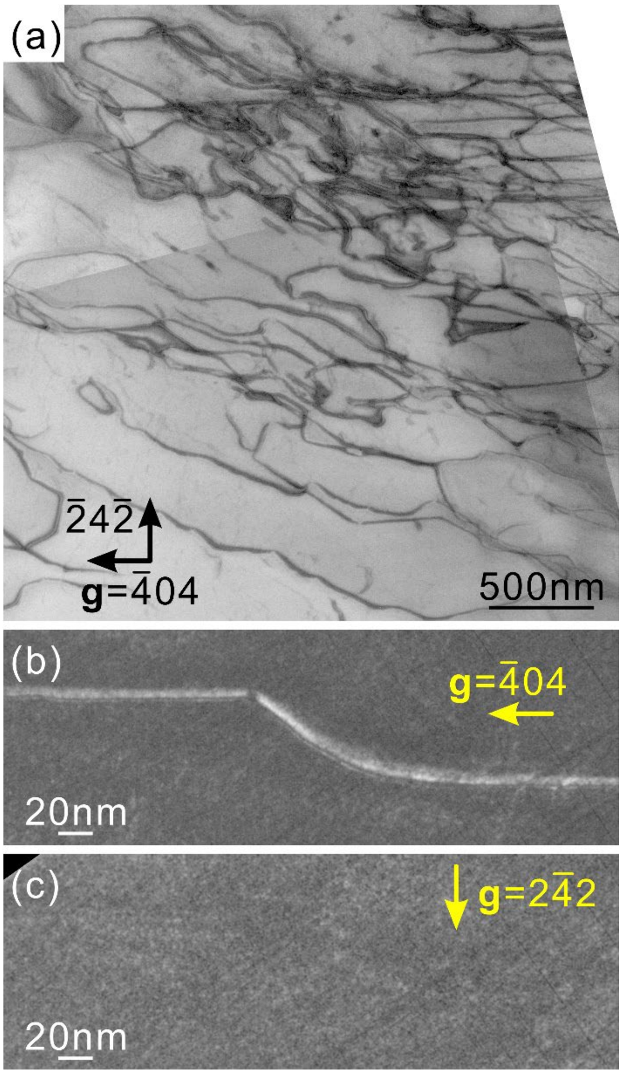

Fig. 4. (a) Bright-field STEM image of dislocation structure observed in a thin foil cut parallel to the (111) slip plane from a $[\bar{2}67]$-oriented micropillar specimen deformed to 3~4% plastic strain. (b) and (c) are weak-beam dark-field TEM images of the same area for dislocations with $\mathbf{b}=1/2[\bar{1}01]$ taken with (b) $\mathbf{g}=\bar{4}04$ and (c) $\mathbf{g}=2\bar{4}2$, respectively.

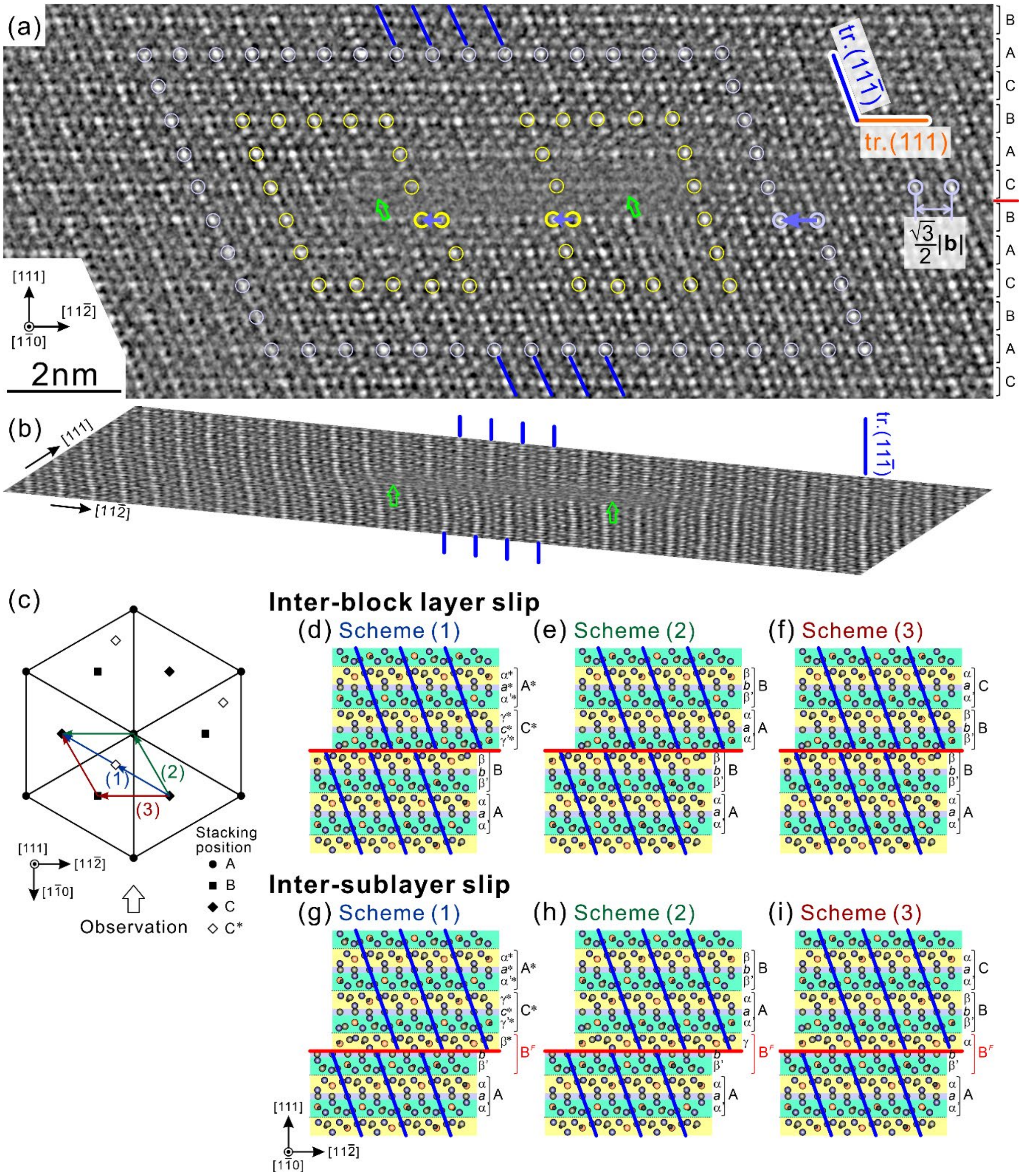

Fig. 5. (a) HAADF-STEM image of the core structure for a 60°-dislocation with **b**=1/2[$\bar{1}$01] introduced in a [$\bar{2}$67]-oriented micropillar specimen deformed to 3~4 % plastic strain. (b) rotated and vertically compressed image of (a) containing the stacking fault between the two partial dislocations with **b**=1/4[$\bar{1}$01]. Schematic illustrations of (c) stacking positions and possible dissociation schemes and (d-i) possible atomic structure of between the two partial dislocations.

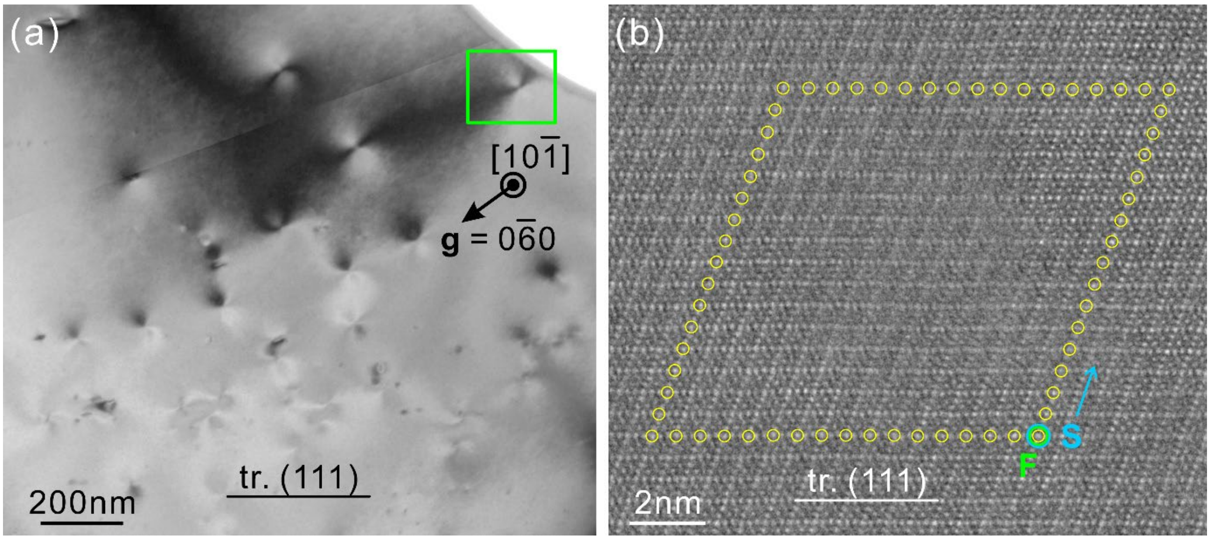

Fig. 6. (a) Bright-field TEM image of screw dislocations in a TEM foil cut perpendicular to the screw orientation $[\bar{1}01]$ from a $[\bar{2}67]$-oriented micropillar specimen deformed to 3~4 % plastic strain. (b) Atomic resolution HAADF-STEM image of a screw dislocation in marked area in (a).

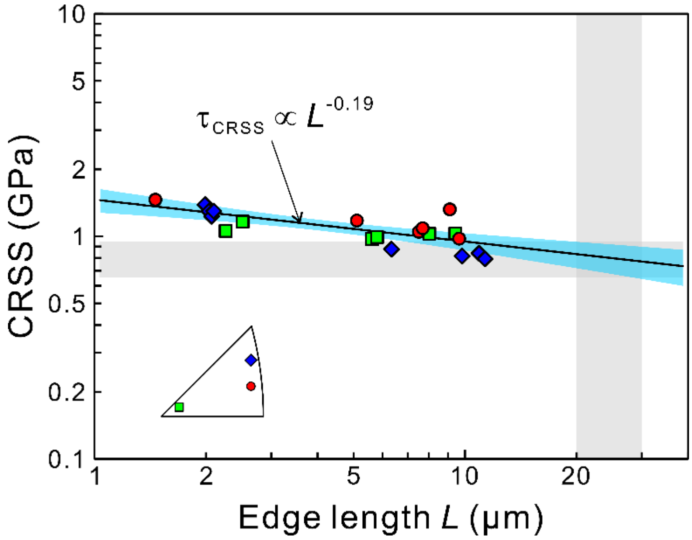

Fig. 7. CRSS values for $(111)[\bar{1}01]$ slip plotted as a function of specimen size. The CRSS values are collected from micropillar single crystals with the three different loading orientations of $[\bar{2}67]$ (red circles), $[\bar{5}89]$ (blue diamonds) and $[\bar{1}\ 2\ 14]$ (green squares). Light blue band corresponds to the 95% confidence band of the power-law fitting.

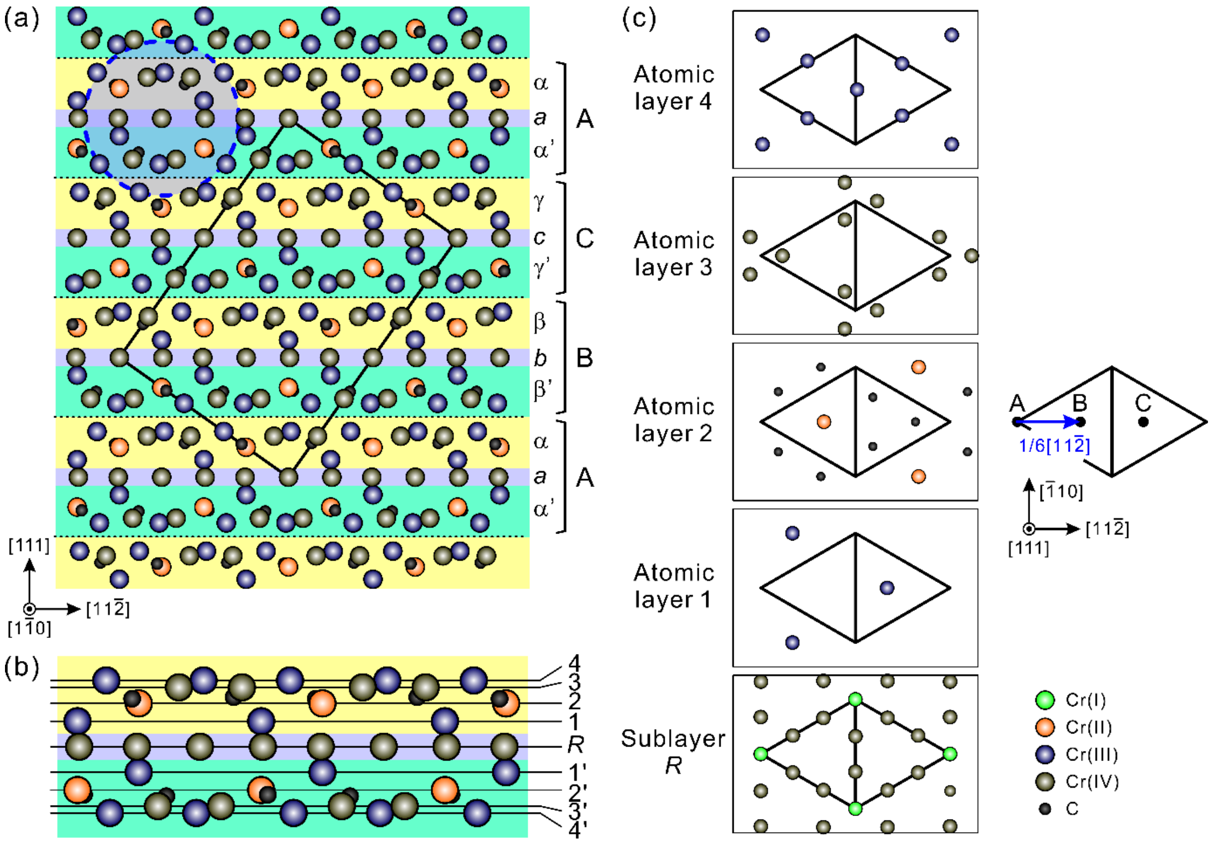

Fig. 8. (a) The $[1\bar{1}0]$ projection of crystal structure of $Cr_{23}C_6$ with the ABC-type stacking of the (111) plane. The outline of the unit cell and a basis attached to a lattice point are indicated with thick black rectangle and blue dotted circle, respectively. (b) Enlargement of the block layer A in (a) with subdivision of a several different parallel (111) planes. (c) Atomic arrangement of each of (111) planes defined in (b).

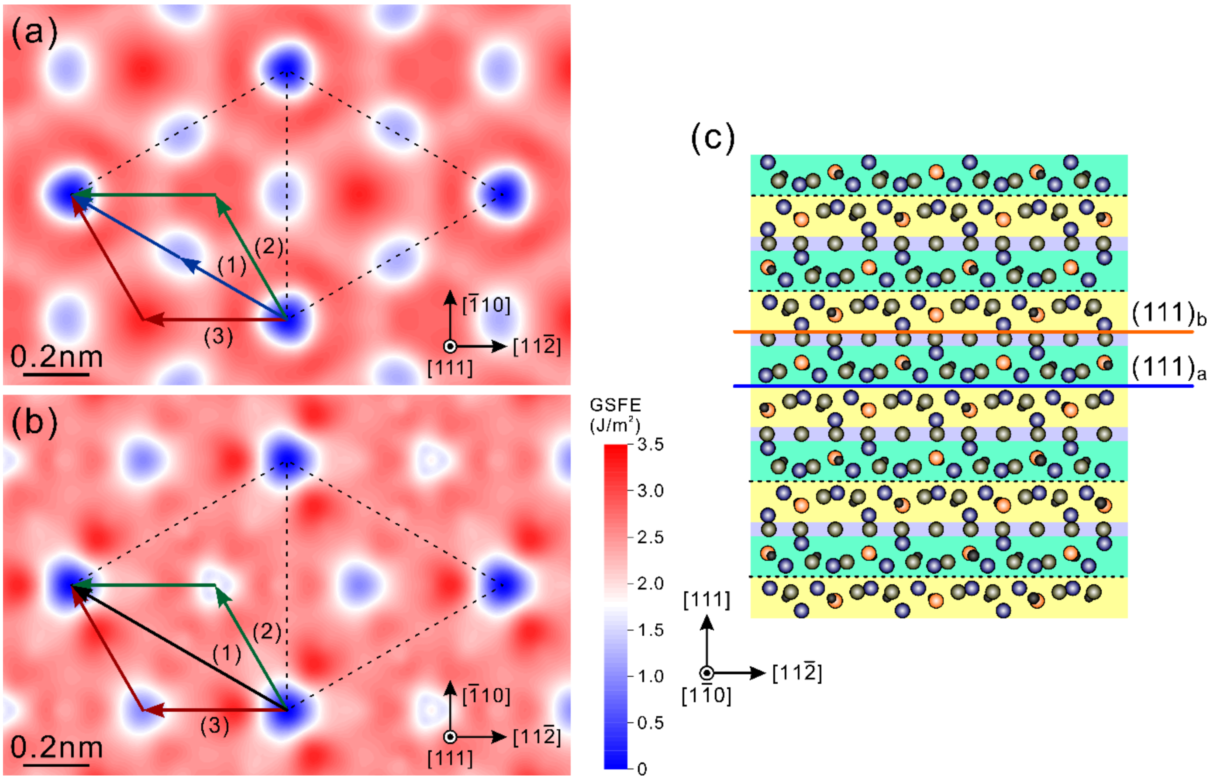

Fig. 9. Generalized stacking fault energy map calculated on (111) for (a) inter-block layer slip and (b) inter-sublayer slip. (c) Schematic illustration of the exact locations of the (111) slip plane for inter-block layer slip ((111)$_a$) and inter-sublayer slip ((111)$_b$).

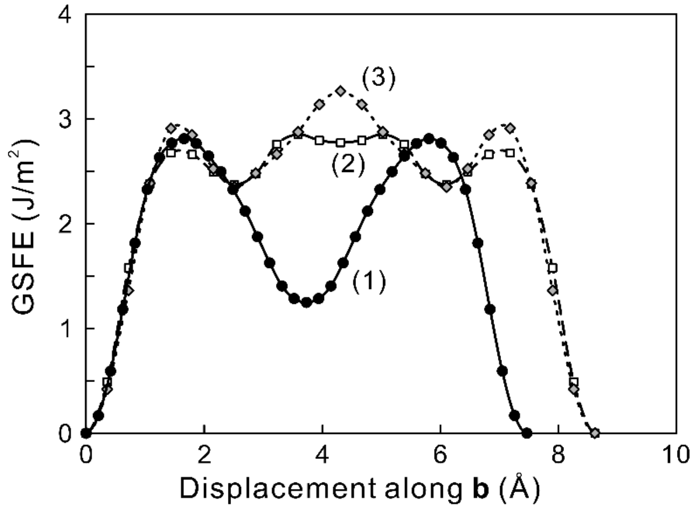
(a) Inter-block layer slip

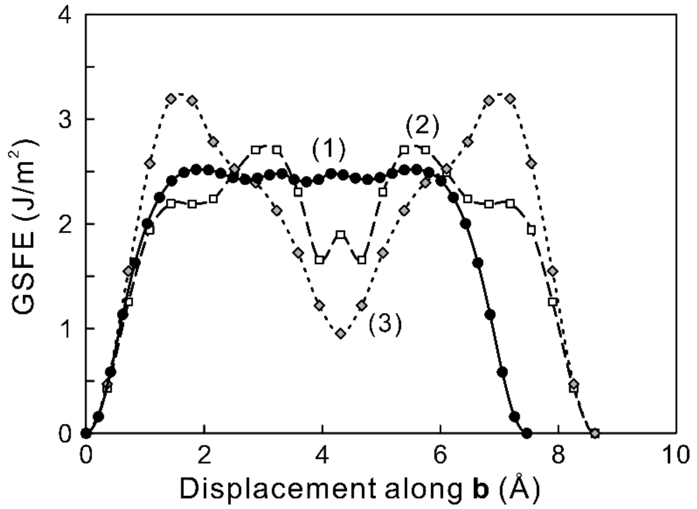
(b) Inter-sublayer slip

Fig. 10. The calculated GSFE-displacement curves along the possible slip directions for (a) inter-block layer slip and (b) inter-sublayer slip.

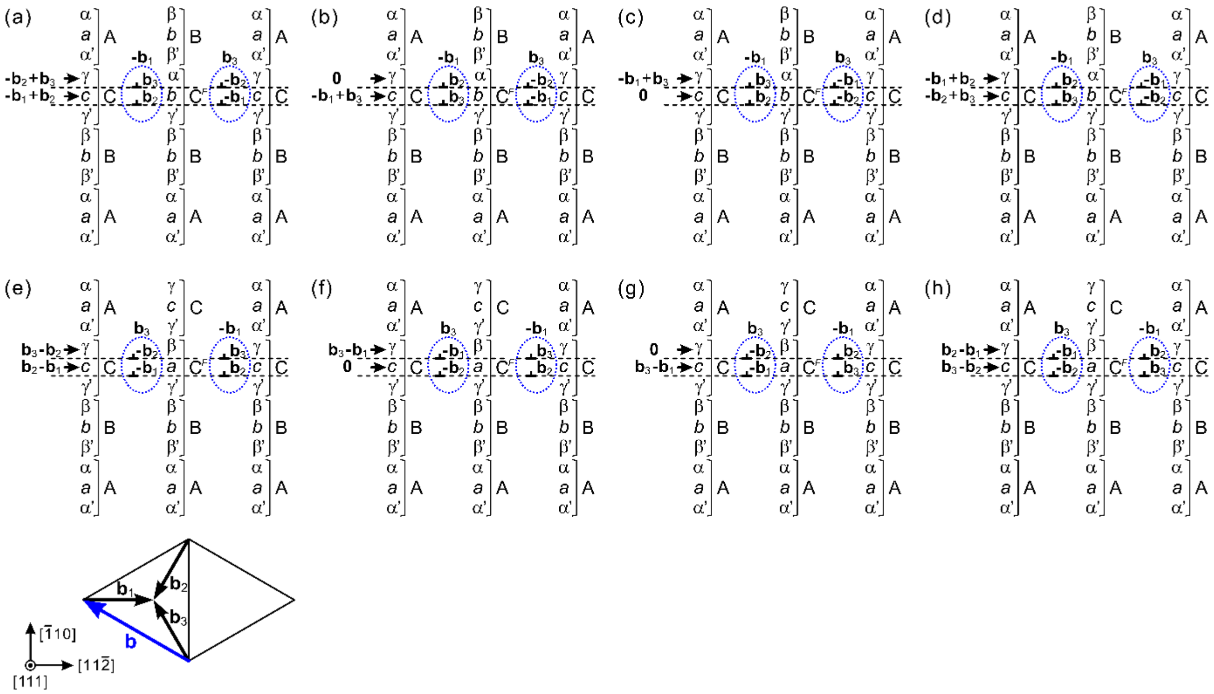

Fig. 11. Possible double-layer stacking faults introduced by synchroshear with eight different combinations of partial Burgers vectors for (a)-(d) inter-block layer slip and (e)-(h) inter-sublayer slip.

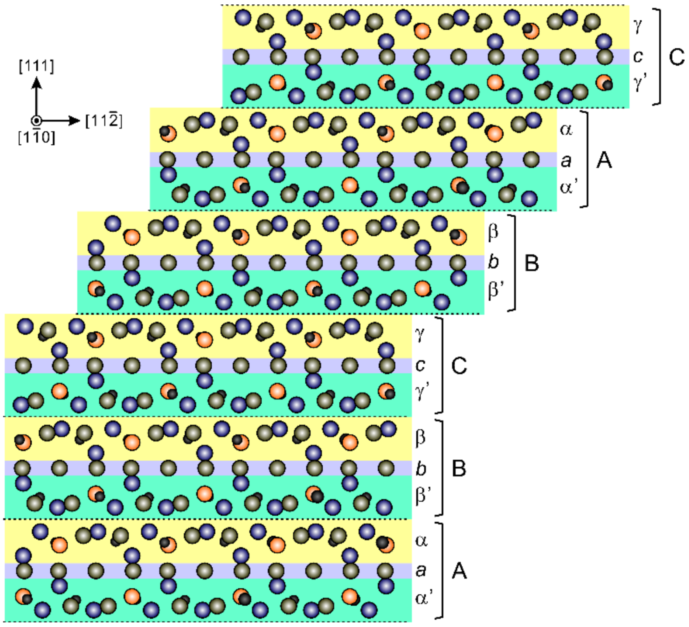

Fig. 12. Atomic structure change after the passage of three Shockley partial dislocations on three successive inter-block layer slip planes.

Supplementary material for

On the inherent strength of $Cr_{23}C_6$ with the complex face-centered cubic $D8_4$ structure

Kyosuke Kishida[1,2,*], Mitsuhiro Ito[1], Haruyuki Inui[1,2], Martin Heilmaier[3], and Gunther Eggeler[4]
[1] Department of Materials Science and Engineering, Kyoto University
Sakyo-ku, Kyoto 606-8501, JAPAN
[2] Center for Elements Strategy Initiative for Structural Materials (ESISM), Kyoto University
Sakyo-ku, Kyoto 606-8501, JAPAN
[3]Institute for Applied Materials (IAM-WK), Karlsruhe Institute of Technology (KIT), Engelbert-Arnold-Strasse 4, 76131 Karlsruhe, Germany
[4]Lehrstuhl Werkstoffwissenschaft (WW), Institut für Werkstoffe, Ruhr-Universität Bochum, Universitätsstrasse 150, D-44780 Bochum, Germany

***Corresponding author e-mail:** kishida.kyosuke.6w@kyoto-u.ac.jp

<Supplementary Figure>

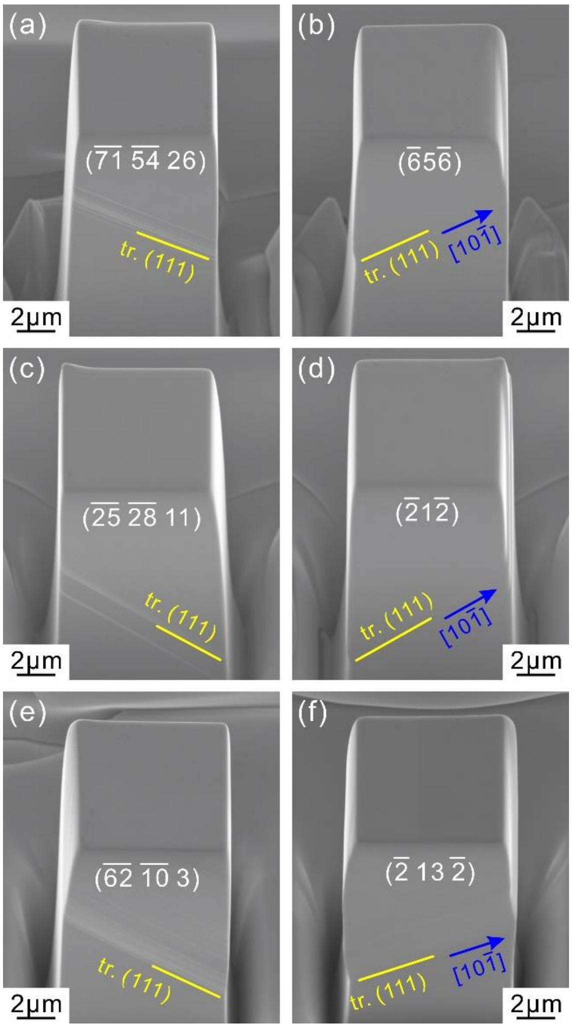

Fig. S1. SEM secondary electron images of side surfaces of deformed micropillar specimens taken diagonally from the above (inclined by 30° from the loading axis) for (a,b) [$\bar{2}67$], (c,d) [$\bar{5}89$] and (e,f) [$\bar{1}\ 2\ 14$] orientations.